PNAS RESEARCH ARTICLE | MEDICAL SCIENCES OPEN ACCESS

Tumor FAK orchestrates immunosuppression in ovarian cancer via the CD155/TIGIT axis

Duygu Ozmadenci[a], Jayanth S. Shankara Narayanan[b], Jacob Andrew[a], Marjaana Ojalill[a], Allison M. Barrie[a], Shulin Jiang[a], Samhita Iyer[a], Xiao Lei Chen[c], Michael Rose[d], Valeria Estrada[d], Alfredo Molinolo[d], Thomas Bertotto[a], Zbigniew Mikulski[e], Michael C. McHale[a], Rebekah R. White[b], Denise C. Connolly[f], Jonathan A. Pachter[g], Vijay K. Kuchroo[h], Dwayne G. Stupack[a], and David D. Schlaepfer[a,1]

Edited by Myles Brown, Dana-Farber Cancer Institute, Boston, MA; received September 17, 2021; accepted March 9, 2022

High-grade serous ovarian cancer (HGSOC) is a lethal malignancy characterized by an immunosuppressive tumor microenvironment containing few tumor infiltrating lymphocytes (TILs) and an insensitivity to checkpoint inhibitor immunotherapies. Gains in the *PTK2* gene encoding focal adhesion kinase (FAK) at Chr8 q24.3 occur in ∼70% of HGSOC tumors, and elevated FAK messenger RNA (mRNA) levels are associated with poor patient survival. Herein, we show that active FAK, phosphorylated at tyrosine-576 within catalytic domain, is significantly increased in late-stage HGSOC tumors. Active FAK costained with CD155, a checkpoint receptor ligand for TIGIT (T cell immunoreceptor with immunoglobulin and immunoreceptor tyrosine-based inhibitory motif domains), in HGSOC tumors and a selective association between FAK and TIGIT checkpoint ligands were supported by patient transcriptomic database analysis. HGSOC tumors with high FAK expression were associated with low CD3 mRNA levels. Accordingly, late-stage tumors showed elevated active FAK staining and significantly lower levels of CD3+ TILs. Using the KMF (Kras, Myc, FAK) syngeneic ovarian tumor model containing spontaneous *PTK2* (FAK) gene gains, the effects of tumor intrinsic genetic or oral small molecule FAK inhibitior (FAKi; VS-4718) were evaluated in vivo. Blocking FAK activity decreased tumor burden, suppressed ascites KMF-associated CD155 levels, and increased peritoneal TILs. The combination of FAKi with blocking TIGIT antibody (1B4) maintained elevated TIL levels and reduced TIGIT+ T regulatory cell levels, prolonged host survival, increased CXCL13 levels, and led to the formation of omental tertiary lymphoid structures. Collectively, our studies support FAK and TIGIT targeting as a rationale immunotherapy combination for HGSOC.

high-grade serous ovarian cancer | immunotherapy | FAK | CD155 | tertiary lymphoid structures

High-grade serous ovarian cancer (HGSOC) is the most lethal gynecologic malignancy in the United States (1). Surgery followed by platinum and paclitaxel chemotherapy is standard of care therapy, but up to 80% of patients develop chemotherapy resistance and succumb to disease within 5 y (2). HGSOC is characterized by p53 tumor suppressor inactivation, widespread genomic gains and deletions, and a highly immunosuppressive tumor microenvironment (3). Tumor-infiltrating T cell accumulation is prognostic for increased HGSOC patient survival, spurring immunotherapeutic approaches designed to counteract HGSOC-mediated T cell suppression (4, 5). However, HGSOC mutational burden is relatively low and different combinations of checkpoint inhibitors remain in clinical trial testing (6). To date, only a small subset of HGSOC patients with microsatellite instability have derived benefit from checkpoint inhibitor immunotherapies (7). Better treatments are needed to counter act tumor immune evasion.

Two well-studied checkpoint receptors, namely, CTLA-4 (cytotoxic T lymphocyte-associated protein 4) and PD-1 (programmed cell death protein 1) suppress T-cell-mediated immune responses (8). However, other coinhibitory receptors also suppress T cell function (9). TIGIT (T cell immunoreceptor with immunoglobulin [Ig] and immunoreceptor tyrosine-based inhibitory motif domain) is expressed on T cells, natural killer cells, regulatory T cells (Tregs), and a subset of B cells (10–13). The TIGIT ligands CD155 (PVR) and CD112 (PVRL2, nectin-2) are abundantly expressed by tumor cells (14, 15). CD155 or CD112 binding to TIGIT can prevent T-cell-mediated tumor elimination (16) and sustain immune evasion (17). CD155 and PD-1 ligand (PD-L1) expression patterns differ in HGSOC, with elevated CD155 levels detected in immunologically "cold" tumors lacking infiltrating lymphocytes (18). Notably, although TIGIT-blocking antibodies show success in some mouse models, human anti-TIGIT clinical trials remain in progress (19, 20).

Significance

High-grade serous ovarian carcinoma (HGSOC) is an immunotherapy-resistant lethal cancer. An HGSOC hallmark is elevated checkpoint pathway ligand expression that limits antitumor immune responses. Computational, preclinical, and patient tumor multiplexed analyses revealed that tumor-associated focal adhesion kinase (FAK) activation regulates CD155 expression, a checkpoint ligand for TIGIT (T cell immunoreceptor with immunoglobulin and immunoreceptor tyrosine-based inhibitory motif domains). Using an aggressive mouse ovarian tumor model, we find that combined oral FAK inhibitor plus function-blocking TIGIT antibody immunotherapy reduced tumor burden, prolonged mouse survival, and led to immune cell activation and tertiary lymphoid structure formation, hallmarks of an antitumor immune response. As FAK is commonly overexpressed in HGSOC tumors, targeting FAK and TIGIT may limit tumor immune evasion.

Competing interest statement: J.A.P. is a current employee at Verastem Inc.

This article is a PNAS Direct Submission.

[1]To whom correspondence may be addressed. Email: dschlaepfer@health.ucsd.edu.

This article contains supporting information online at http://www.pnas.org/lookup/suppl/doi:10.1073/pnas.2117065119/-/DCSupplemental.

Published April 25, 2022.

The development of immunotherapies for HGSOC has encountered setbacks, due in part to a lack of syngeneic murine models that recapitulate human disease (21, 22). Recently, genetically engineered murine fallopian-tube-derived epithelial cells that form tumors in mice have yielded insights into potential chemotherapy and immunotherapy sensitivities (23, 24). KMF (Kras, Myc, focal adhesion kinase [FAK]) cells are an aggressive, ID8-derived ovarian cancer model (25) displaying in-vivo-acquired platinum resistance and additional genetic changes mirroring HGSOC, including gains in the *Kras*, *Myc*, and *Ptk2* (FAK) genes (26). KMF cells express high levels of proliferation, pluripotency, and DNA repair markers and thus provide additional ovarian tumor modeling opportunities of HGSOC disease in immune-competent C57Bl6 mice.

The human *PTK2* gene at Chr8 q24.3, encoding FAK, is frequently amplified in gynecologic tumors (27). FAK is a protein tyrosine kinase that serves as a signaling hub that can protect tumor cells from stress induced by chemo- and other cytotoxic therapies (27). In HGSOC, an elevated FAK transcript is associated with a poor patient prognosis (26). Phosphospecific antibodies to the FAK Y397 autophosphorylation site are commonly used as markers of FAK activity (28). FAK Y397 phosphorylation is elevated within Pax8-positive HGSOC tumor cells and is increased in tumors after neoadjuvant carboplatin plus paclitaxel chemotherapy, suggesting a role for FAK in chemotherapy resistance (26, 29). Other tumor types exhibit FAK Y397 phosphorylation in both stromal and tumor cells (30–32). In pancreatic cancer models, FAK inhibitior (FAKi)-enhanced responsiveness to checkpoint inhibitor immunotherapy occurs in part by decreasing fibrosis (33). In a squamous cell carcinoma model, tumor-intrinsic FAK activity promoted chemokine expression limiting CD8+ T cell responses (34, 35). In both mouse models, FAKi treatment enhanced anti-PD-1 inhibitory effects, and currently, clinical trials are testing orally available small-molecule FAKis with anti-PD1 therapeutics (27).

Herein, we identify active FAK and CD155 as markers of immune-evasive HGSOC tumors. Bioinformatic analyses revealed a positive association between CD112 and CD155 with FAK in HGSOC. Using a validated antibody marker of FAK activity in multiplex staining, we find that active FAK, phosphorylated at Y576 within the catalytic domain, is associated with increased CD155 expression. In the mouse KMF ovarian tumor model, genetic or oral small-molecule FAK inhibition reduced KMF CD155 expression and increased lymphocyte infiltration, revealing a tumor-intrinsic role for FAK in promoting immunosuppression. FAKi plus a TIGIT-blocking antibody significantly reduced tumor burden and increased host survival associated with elevated CXCL13 production and tertiary lymphoid structure (TLS) formation. These studies, revealing a linkage between active FAK, CD155, and TIGIT, merit future consideration for HGSOC immunotherapy combinations.

Results

FAK and TIGIT Ligand Coexpression Revealed by HGSOC Transcriptome Analyses. HGSOC immune suppression is orchestrated by tumor cells. Since elevated FAK messenger RNA (mRNA) levels parallel *PTK2* gains in HGSOC (26), we explored whether checkpoint receptor ligands may show an association with *PTK2* (FAK) at the mRNA level. Bioinformatic analyses of The Cancer Genome Atlas (TCGA) Ovarian Serous Cystadenocarcinoma (TCGA Firehose Legacy) dataset revealed an association between FAK and CD112 or CD155 but not with other checkpoint receptor ligands in HGSOC ($n = 182$, Pearson scores greater than 0.2) (Fig. 1*A*). FAK and CD155 mRNA were also weakly associated in breast and pancreatic carcinoma but not in lung carcinoma or neuroblastoma (*SI Appendix*, Fig. S1*A*). To determine whether HGSOC FAK levels are related to intratumoral T cell presence, FAK mRNA levels were binned from low to high expression and compared to CD3, a marker of lymphocytes (Fig. 1*B*). CD3 mRNA expression was inversely associated with FAK. In contrast, the Pax8 ovarian tumor marker remained constant across the FAK low to FAK high tumor groups (*SI Appendix*, Fig. S1*B*). The link between tumor FAK and CD12 and CD155 TIGIT ligands and the inverse relationship between tumor FAK and CD3 transcripts implicates FAK as a potential regulator of the HGSOC immune microenvironment.

Active FAK (FAK pY576) and CD155 Coexpression in HGSOC Tumor Microarrays by Multiplex Immunofluorescence Staining. Phosphospecific antibodies to the FAK Y397 (pY397 FAK) autophosphorylation site can be used to stain frozen sections of breast and ovarian tumors (26, 30). However, paraffin-embedded HGSOC tumor staining with these FAK pY397 antibodies in multiplex analyses was hampered by nonspecific staining. Therefore, we next tested phospho-specific antibodies to FAK tyrosine 576 (pY576 FAK), which recognize catalytic domain phosphorylation upon FAK activation (28). As a control, we used a R454K FAK point mutant that renders FAK catalytically inactive (kinase dead [KD]) (Fig. 1*C*). Subsequent immunoblotting using cells expressing FAK wildtype (WT), FAK-KD, FAK-Y576F mutated, or FAK-Y397F mutated proteins confirmed FAK pY397 and FAK pY576 phosphospecific antibody specificity (Fig. 1*D*). FAKi (VS-4718) treatment of KMF tumor cells prevented both FAK Y397 and FAK Y576 phosphorylation (*SI Appendix*, Fig. S1*C*). Oral FAKi (VS-4718, 100 mg/kg) administration to human-ovarian-tumor-bearing mice reduced FAK pY576 but not total FAK staining in paraffin sections (*SI Appendix*, Fig. S2), thereby validating the use of FAK pY576 antibodies as an active FAK marker.

To evaluate expression patterns of active FAK (pY576 FAK), CD155, and CD3, human ovarian tumor tissue microarrays (TMAs) were analyzed by multiplex immunofluorescence staining (Fig. 1*E*). Anti-CD3 staining detected both individual cells and clusters of cells in tissue areas distinct from active FAK staining. High levels of active FAK staining were observed in multiple regions of advanced-stage HGSOC tumors (Fig. 1 *E* and *F*) and costained with the Pax8 tumor marker (*SI Appendix*, Fig. S1*D*). Digital image quantification showed significantly higher active FAK staining among stage III+IV relative to stage I+II tumors (Fig. 1*G*). CD155 staining was significantly greater among cells with high FAK activity (Fig. 1*H* and *SI Appendix*, Fig. S1*D*). Conversely, stage III+IV tumors had lower overall levels of CD3 staining when compared with stage I+II tumors (Fig. 1*I*), consistent with prior HGSOC clinical studies (36). Together, a positive association between active FAK and CD155 expression was detected that may negatively impact CD3+ tumor infiltrating lymphocyte (TIL) accumulation.

T Cell Activation Markers Are Elevated upon Genetic or Pharmacologic FAK Inhibition in KMF Tumor Ascites. KMF tumor cells can be recovered from ascites (plus peritoneal wash) together with immune infiltrate after intraperitoneal (IP) seeding of C57Bl6/N mice (26). Previously, studies with FAK knockout (KO), and green fluorescent protein (GFP)-FAK-WT or GFP-FAK-KD reconstituted cells, revealed that FAK activity

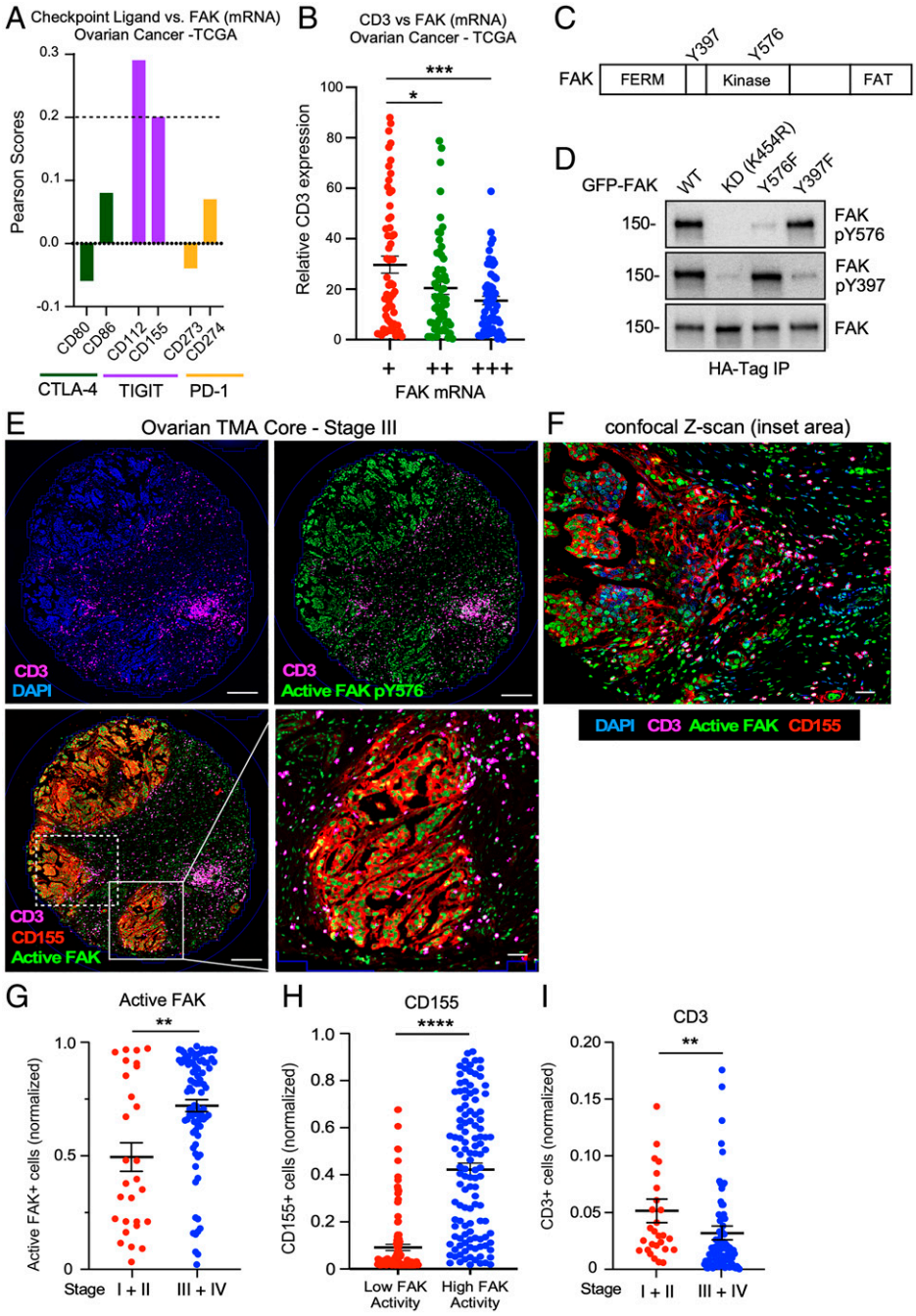

Fig. 1. Active FAK and CD155 coexpression in HGSOC tumor regions with low CD3 T cell infiltration. (*A*) Coexpression of FAK (*PTK2*) and ligands for CTLA-4 (CD80, CD86), TIGIT (CD112, CD155), and PD-1 (CD273, CD274) mRNAs among patients in the TCGA Ovarian Serous Cystadenocarcinoma database (n = 182) as analyzed by Pearson Product-Moment Correlation. Values of 0.2 or greater support an association. (*B*) Comparisons of CD3 versus FAK mRNA in tumors grouped for increasing FAK mRNA expression (+, ++, and +++). Data are mean ± SEM (one-way ANOVA with Tukey's multiple comparisons test [$*P < 0.05$, $***P < 0.001$]). (*C*) FAK protein schematic. Point mutation at FAK Lys (K)-454 to arginine (R) renders FAK KD. (*D*) GFP fusions of FAK-WT, FAK-KD (K454R), FAK-Y576F, or FAK-Y397F containing a hemagglutinin (HA) epitope-tag were immunoprecipitated and immunoblotted with phosphospecific antibodies to FAK Y576, to FAK Y397, and total FAK. (*E*) Representative multiplex immunofluorescence (IF) staining of a paraffin-embedded HGSOC tumor tissue microarray (TMA) core. Shown is a stage III TMA core sequentially stained for active FAK (pY576 FAK, green), CD155 (red), CD3 (magenta), and DAPI (blue) (Scale bar, 200 μm.) *Bottom Right*, magnified *Inset* solid boxed in *Bottom Left* (Scale bar, 50 μm). (*F*) Laser confocal scan of dashed box shown in *E, Bottom Left*. (Scale bar, 50 μm.) (*G*) Cells of stage III+IV HGSOC tumors contain significantly more active FAK (pY576 FAK) compared to stage I+II HGSOC tumors. Data are mean ± SEM ($**P < 0.01$, Mann–Whitney *U* test). Normalized data are the number of FAK pY576 positive to total cells. (*H*) Greater CD155 expression in HGSOC cells with high versus low FAK activity as determined by FAK pY576 costaining. Data are mean ± SEM ($****P < 0.0001$, Mann–Whitney *U* test). Ratio for low FAK activity is the number of CD155 positive to total cells. Ratio for high FAK activity is the number of CD155 and pFAK Y576 double positive to total cells. (*I*) Significantly fewer CD3+ cells in stage III+IV compared to stage I+II HGSOC tumors. Data are mean ± SEM ($**P < 0.01$, Mann–Whitney *U* test). Normalized data are the number of CD3 positive to total cells. (*G–I*) A total of 119 cores from 60 patients were quantified (n = 12,689 cells, in a range of 4,584 to 31,246 per core). QuPath (0.2.3) (50) was used for image analyses.

sustained KMF platinum resistance and in vitro tumorsphere formation via β-catenin signaling (26). However, active β-catenin was insufficient to promote KMF FAK-KO tumor growth in vivo. To better understand the role of FAK activity in vivo, we evaluated changes in ascitic KMF cells and associated TILs of mice seeded with luciferase-labeled GFP-FAK-WT or GFP-FAK-KD tumor cells (Fig. 2*A*). In parallel, oral FAKi administration was assessed for effects on GFP-FAK-WT

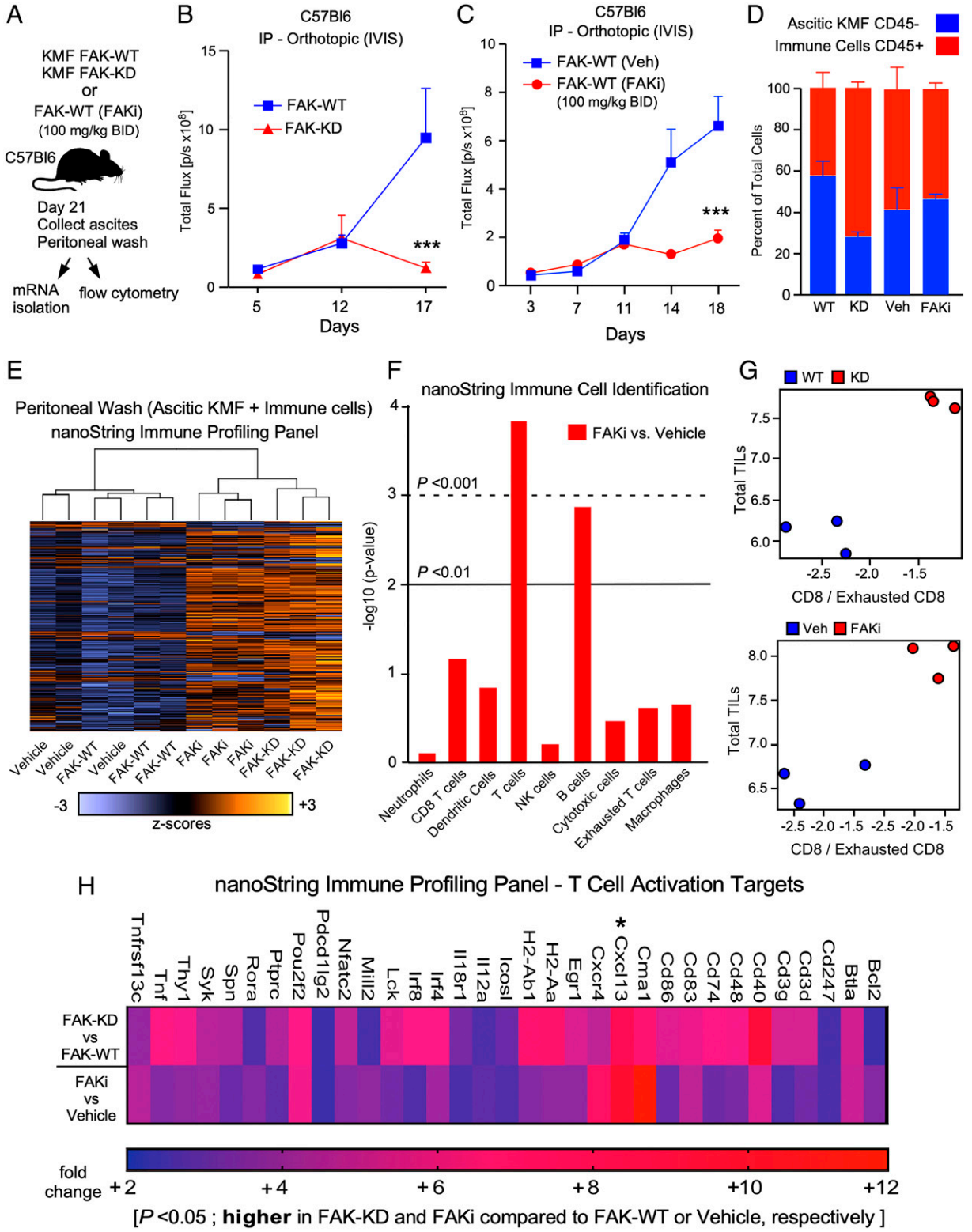

Fig. 2. Genetic or pharmacologic FAK inhibition increases T cell activation mRNAs in infiltrating lymphocytes in an ascitic syngeneic mouse ovarian cancer model. (*A*) Experimental schematic: Luciferase-labeled GFP-FAK-WT or GFP-FAK-KD reconstituted KMF cells were injected (seeded) into the IP cavity of C57Bl6/N mice, and at day 21, KMF and infiltrating leukocytes were collected by peritoneal wash. GFP-FAK-WT-seeded mice were orally administered FAK inhibitor (FAKi) VS-4718 (100 mg/kg, BID) for 20 d prior to cell collection. (*B*) In vivo imaging system (IVIS) imaging of mice with KMF FAK-WT or KMF FAK-KD cells. Values are means ± SEM ($n = 4$ to 6 mice per group, one-way ANOVA with Tukey's multiple comparisons test (***$P < 0.001$). (*C*) IVIS imaging of vehicle or FAKi (100 mg/kg, BID) treated KMF FAK-WT seeded mice. Values are means ± SEM ($n = 9$ or 10 per group, ***$P < 0.001$, unpaired t test). (*D*) Percentage of peritoneal CD45- tumor (blue) and CD45+ lymphocyte (red) ascites cells recovered at day 21. Values are means ± SEM. (*E*) The nanoString Immune Profiler panel was used to analyze mRNA from peritoneal collected cells (day 21) of FAK-WT, FAK-KD, and FAK-WT with FAKi or vehicle treated tumor-bearing mice ($n = 3$ independent isolates per group, shown individually), and heatmaps were generated using nCounter Advanced Analysis Software. (*F*) Predicted immune cell types associated with nanoString mRNA changes ($n = 3$ per group) in vehicle versus FAKi-treated tumor-bearing mice. Significance values are −log10 transformed and were determined using an alpha of 0.01. (*G*) Ratio of CD8 to exhausted CD8 T cell markers and TILs are higher in tumor-bearing mice upon FAK inhibition. (*H*) Elevated T-cell-associated mRNAs in FAK-KD vs. FAK-WT and in FAKi-treated vs. vehicle KMF tumor-bearing mice. Range is 2- to 12-fold increased with a t test P value minimum, $P < 0.05$. Indicated is *Cxcl13, elevated 10-fold or more in FAK-KD and FAKi groups.

tumor-bearing mice. By Day 17, luminescence imaging revealed that tumor burden was significantly lower in FAK-KD compared to FAK-WT mice and upon oral FAKi administration compared to vehicle control, respectively (Fig. 2 *B* and *C*). At Day 21, ascites and peritoneal wash collected cells were analyzed by flow cytometry (Fig. 2*D* and *SI Appendix*, Figs. S3 and S4). As expected, KMF tumor cells were CD45 negative (−) and GFP-positive (+). No CD45- cells were detected by flow cytometry in peritoneal washes from mice without KMF seeding (*SI Appendix*, Fig. S3). Notably, genetic or pharmacological FAK inhibition reduced the number of ascitic CD45- KMF cells recovered 5- to 10-fold (*SI Appendix*, Fig. S5) and genetic but not pharmacologic FAK inhibition altered the ascitic CD45- to CD45+ immune cell ratio (Fig. 2*D*). A parallel analysis of omental metastases revealed fewer and smaller tumor implants in FAK-KD and FAKi-treated mice compared to FAK-WT and vehicle, respectively (*SI Appendix*, Fig. S6). After IP seeding, the KMF model allows for rapid recovery and analysis of both tumor and immune cells within the IP tumor microenvironment.

We next performed nanoString mRNA Immune Profiling Panel comparisons. Heat-map clustering analysis revealed that FAK-KD and FAKi treatments grouped together, away from their respective controls (Fig. 2*E*). Notably, these parallel changes in transcript expression arose from independent approaches to suppress FAK activity. A cluster of T cell transcripts were significantly increased upon FAK inhibition (Fig. 2*F*). Pattern analysis (nSolver) algorithms revealed an increase in total TILs and an increase in the CD8-to-exhausted CD8 ratio among both FAKi and FAK-KD experimental groups compared to respective controls (Fig. 2*G*). These results implicate KMF FAK as a negative regulator of T cell infiltration and a potential promoter of T cell exhaustion. Differentially expressed gene ratios calculated by nSolver identified 77 genes that were significantly elevated at least twofold in both FAK-KD and FAKi treatment groups compared to controls. Of these, 33 were T cell activity markers that were elevated from 2- to 12-fold upon FAK inhibition (Fig. 2*H*). This included CXCL13, a chemokine that is an independent beneficial prognostic marker in HGSOC (37). Together, these results link KMF FAK activity to the suppression of T cell responses.

KMF FAK Activity Promotes CD155 Expression and Represses T Cell Infiltration. To evaluate cell-specific changes in KMF ascites, flow cytometry analysis was performed on gated subpopulations (*SI Appendix*, Figs. S3 and S4) of CD45− (>95% GFP+ KMF tumor) and CD45+ leukocytes. At day 21, FAK-KD ascitic cells displayed reduced levels of checkpoint receptor PD-L1, CD112, and CD155 ligands relative to KMF FAK-WT cells in vivo (Fig. 3 *A*–*D*). Significant decreases in the infiltration of T regulatory cells (Tregs), granulocytes, and monocytes occurred in FAK-KD compared to FAK-WT ascites (Fig. 3 *E*–*G*). Elevated infiltration of CD8+ and CD4+ T cells were detected in ascites of FAK-KD compared to FAK-WT (Fig. 3 *H* and *I*), and in parallel, increased CD3 staining was observed nearby FAK-KD but not FAK-WT omental metastases (*SI Appendix*, Fig. S6). Importantly, PD-1 and TIGIT exhaustion markers were reduced on CD8+ T cells in FAK-KD compared to FAK-WT ascites (Fig. 3 *J*–*L*). Together, these results show that genetic KMF FAK inhibition results in increased TIL recruitment and decreased T cell exhaustion marker levels.

FAK and TIGIT Inhibition Decrease Immunosuppressive Cell Populations. Since genetic FAK inhibition attenuated CD112 and CD155 expression on KMF cells in vivo (Fig. 3), we tested the combination of oral FAKi (VS-4718) administration with a TIGIT-blocking antibody (monoclonal antibody [mAb] 1B4) (38), reasoning that FAKi primarily targets KMF tumors, while anti-TIGIT acts on immune cells (Fig. 4). Oral FAKi treatment reduced ascitic KMF cell number, whereas anti-TIGIT treatment did not (Fig. 4*A*). FAKi treatment resulted in the loss of PD-L1, with significant reductions of CD112 and CD155 expression on ascitic KMF CD45− cells compared to vehicle (Fig. 4 *B*–*D*). By contrast, anti-TIGIT reduced CD112, but not CD155 levels on CD45− ascitic KMF cells (Fig. 4 *C* and *D*).

TIGIT antibody treatment alone did not alter CD8+ T cell abundance or PD-1 expression on CD4+ and CD8+ T cells (Fig. 4 *E*–*H*). In contrast, FAKi treatment increased CD8+ (Fig. 4*E*) and CD4+ (Fig. 4*G*) TILs, with corresponding suppression of PD-1 (Fig. 4 *F* and *H*). Anti-TIGIT treatment decreased TIGIT receptor levels on CD4+ but not CD8+ T cells relative to controls (Fig. 4 *I* and *J*). It is noted that the 1G9 antibody used for TIGIT detection may recognize an overlapping epitope with the 1B4 anti-TIGIT function-blocking antibody (16, 38). However, we find that day 11 agonistic injection of 1B4 does not prevent 1G9 detection of TIGIT on CD8+ TILs at day 21 (Fig. 4*I*). Notably, either FAKi or FAKi plus anti-TIGIT reduced both PD-1 and TIGIT levels on infiltrated CD4+ and CD8+ T cells (Fig. 4 *E*–*J*). FAKi plus anti-TIGIT also reduced the percentage of granulocytes, monocytes, and macrophages in ascites but did not alter dendritic cell percentage relative to controls (*SI Appendix*, Fig. S7). Importantly, Treg abundance in ascites was decreased by both FAKi alone and FAKi plus anti-TIGIT compared to vehicle control (Fig. 4*K*).

Tregs function to suppress the immune response. Lowering TIGIT levels on Tregs is important in limiting Treg function (12). While FAKi reduced Treg TIGIT levels, anti-TIGIT alone or FAKi plus anti-TIGIT dramatically lowered Treg TIGIT receptor expression (Fig. 4*L*). Since TIGIT expression on helper and cytotoxic T cells is a marker of exhaustion (12, 39) and this was reduced by FAKi or anti-TIGIT plus FAKi, our results support complimentary roles for FAKi and anti-TIGIT treatments. Specifically, FAKi promoted T cell infiltration and broadly decreased Tregs and TIGIT expression on CD8+ T cells, while the combination of FAKi plus anti-TIGIT effectively lowered Treg TIGIT levels.

Targeting FAK and TIGIT Enhances Survival and Promotes TLS Formation. IP-seeded KMF tumor cells grow aggressively, and humane endpoints are reached by 4 to 5 wk (26). To evaluate treatment effects on host survival, mice were seeded with KMF FAK-WT cells and subjected to vehicle plus mouse IgG1 isotype control antibody (V), FAKi plus IgG control (oral twice daily [BID], 100 mg/kg), anti-TIGIT antibody plus vehicle (200 μg at days 3, 7, and 11), or FAKi plus anti-TIGIT therapies. Mice were treated for 21 d and then evaluated daily for up to day 65 for tumor burden (Fig. 5*A*). All vehicle control mice reached a humane endpoint by day 28. Although anti-TIGIT treatment alone was associated with a fraction of mice surviving past 40 d, this was not significantly different from the vehicle (Fig. 5*A*). FAKi treatment promoted survival beyond 48 d (Fig. 5*A*). Total ascitic cells collected at day 21 from FAKi-treated mice possessed fourfold-elevated CXCL13 mRNA as determined by qPCR compared to the vehicle (Fig. 5*B*). However, no CXCL13 transcript was detected in flow-sorted ascitic CD45− KMF cells, implicating immune cells in CXCL13 mRNA production upon FAKi treatment. Furthermore, the combination of FAKi plus anti-TIGIT

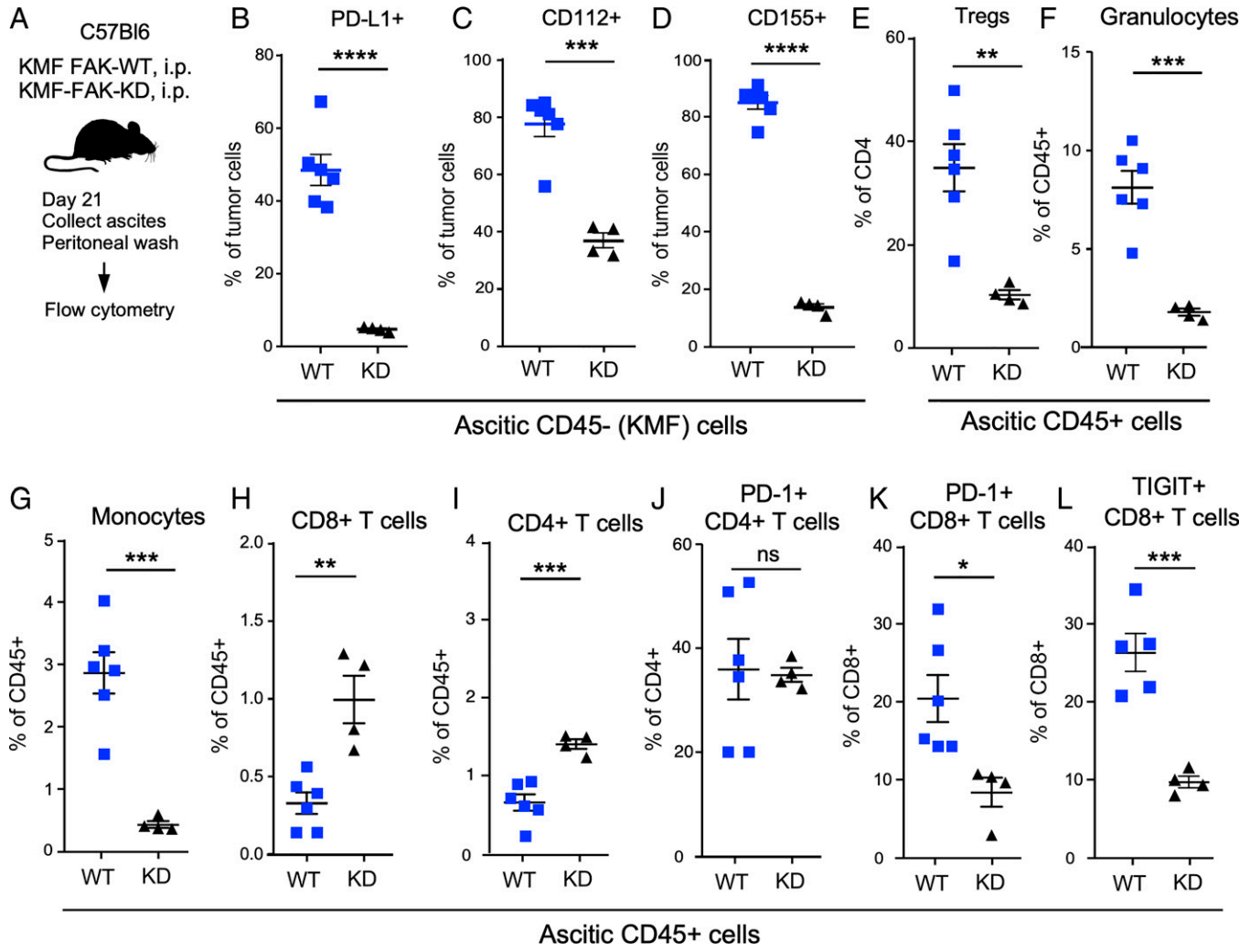

Fig. 3. Tumor FAK activity sustains PD-L1, CD122, and CD155 expression; represses CD4+ and CD8+ T cell infiltration; and promotes PD-1 and TIGIT immunosuppressive populations. (*A*) Experimental schematic: GFP-FAK-WT or GFP-FAK-KD cells were injected IP into C57Bl6/N mice, and at day 21, ascitic KMF cells and infiltrating leukocytes were collected by peritoneal wash and processed for flow cytometry. Percentage of CD45- PD-L1+ (*B*), CD45- CD112+ (*C*), and CD45- CD155+ (*D*) ascitic KMF cells. Percentage of CD45+TCRβ+CD4+CD25+Foxp3+ Tregs (*E*). Percentage of CD45+CD11b+Ly6G+ granulocytes (*F*). Percentage of CD45+CD11b+Ly6G−, Ly6C+ monocytes (*G*). Percentage of CD45+TCRβ+CD8+ T cells (*H*). Percentage of CD45+TCRβ+CD4+ T cells (*I*). Percentage of CD45+TCRβ+CD4+PD-1+ T cells (*J*). Percentage of CD45+TCRβ+CD8+PD-1+ T cells (*K*). Percentage of CD45+TCRβ+CD8+TIGIT+ T cells (*L*). Points shown are individual mice, and values are the means ± SEM (*$P < 0.05$, **$P < 0.01$, ***$P < 0.001$, ****$P < 0.0001$; ns, not significant; unpaired *t* test). Data are representative of three independent experiments.

significantly increased mouse survival beyond 60 d (Fig. 5*A*). In parallel, FAKi plus anti-TIGIT increased CXCL13 levels sevenfold compared to vehicle or to anti-TIGIT alone (Fig. 5*B*). These results are complemented by a Kaplan-Meier analysis showing higher CXCL13 mRNA levels associated with significantly longer HGSOC patient survival (Fig. 5*C*).

One mechanism associated with increased CXCL13 expression and prognostic benefit is the formation of tumor-adjacent TLSs, which are proposed to mediate key antitumor immune responses (40–42). Sequential sectioning and hematoxylin and eosin (H&E) staining of omental tissue collected at day 21 from tumor-bearing and FAKi plus anti-TIGIT–treated mice revealed TLS formation within and nearby necrotic omental metastases (Fig. 5*D*). TLSs were present in all FAKi plus anti-TIGIT–treated mice, in 20% of FAKi, and in 20% of anti-TIGIT but not in vehicle-treated mice (Fig. 5*E*). Multiplex staining revealed an enrichment for B (anti-B220) and T (anti-CD3) cells within omental TLSs (Fig. 5*E*). In all FAKi plus anti-TIGIT–treated mice, smaller (<500 μm) and CD3-positive nonclassical TLSs were also identified adjacent to omental metastases (*SI Appendix*, Fig. S8*A*). Multiplex staining revealed clusters of T and B cells colocalized with immunohistochemical CXCL13 staining within nonclassical omental TLSs (*SI Appendix*, Fig. S8*B*). Collectively, de novo TLS formation and increased CXCL13 with enhanced host survival in the aggressive KMF ovarian tumor model support the notion that combined FAK and TIGIT inhibition may have potential therapeutic benefit to HGSOC patients.

Discussion

HGSOC recurrence and chemotherapy resistance limit 5-y survival, as immunotherapeutic or precision medicine development for this disease remains an unmet challenge. Here, we show that tumor-intrinsic genetic or small-molecule FAK inhibition decreased checkpoint receptor ligand PD-L1, CD112, and CD155 expression on KMF cells, while decreasing Tregs and increasing TILs in an aggressive ascites-generating syngeneic ovarian tumor model. Our results find that tumor FAKi reprogramed the immunosuppressive KMF ascites microenvironment into a TIGIT checkpoint inhibitor-responsive state.

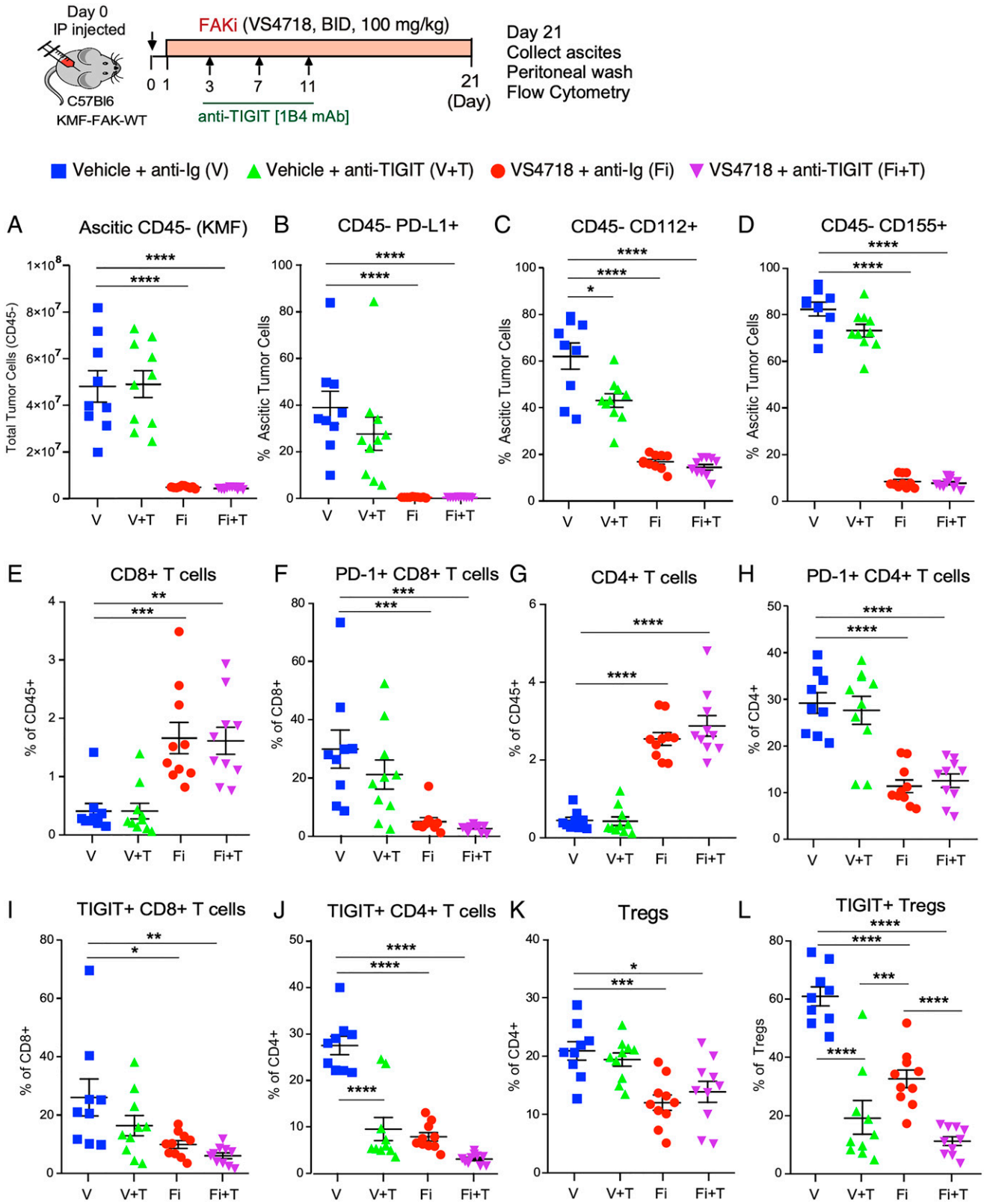

Fig. 4. Oral small-molecule FAK inhibitor plus anti-TIGIT inhibitory antibody reverse KMF ovarian immune suppression. Experimental schematic: GFP-FAK-WT cells were IP seeded in C57Bl6/N mice (day 0). Experimental groups (n = 9 or 10 each) were oral vehicle plus anti-Ig (Ig; V, blue square), vehicle plus anti-TIGIT (mAb 1B4) IP injections (V+T, green triangle), VS-4718 FAK inhibitor (100 mg/kg, BID started at day 1) and anti-Ig (Fi, red circle), or FAKi plus anti-TIGIT (Fi+T, purple triangle). Anti-Ig or anti-TIGIT injections were performed on days 3, 7, and 11. At day 21, KMF tumor and infiltrating leukocytes were collected by peritoneal wash (labeled as ascites) and processed for flow cytometry. (*A*) Tumor cell counts were calculated by multiplying the percentage of CD45− cells by the number of total peritoneal cells collected. Percentage of CD45− PD-L1+ (*B*), CD45− CD112+ (*C*), and CD45− CD155+ (*D*) KMF tumor cells. Percentage of CD45+TCRβ+CD8+ T cells (*E*). Percentage of CD45+TCRβ+CD8+PD-1+ T cells (*F*). Percentage of CD45+TCRβ+CD4+ T cells (*G*). Percentage of CD45+TCRβ+CD4+PD-1+ T cells (*H*). Percentage of CD45+TCRβ+CD8+TIGIT+ T cells (*I*). Percentage of CD45+TCRβ+CD4+TIGIT+ T cells (*J*). Percentage of CD45+TCRβ+CD4+CD25+Foxp3+ Tregs (*K*). Percentage of CD45+TCRβ+CD4+CD25+Foxp3+TIGIT+ Tregs (*L*). Points shown are individual mice, and values are the means ± SEM (*P < 0.05, **P < 0.01, ***P < 0.001, ****P < 0.0001; one-way ANOVA with Tukey's multiple comparisons test). Data are representative of two independent experiments.

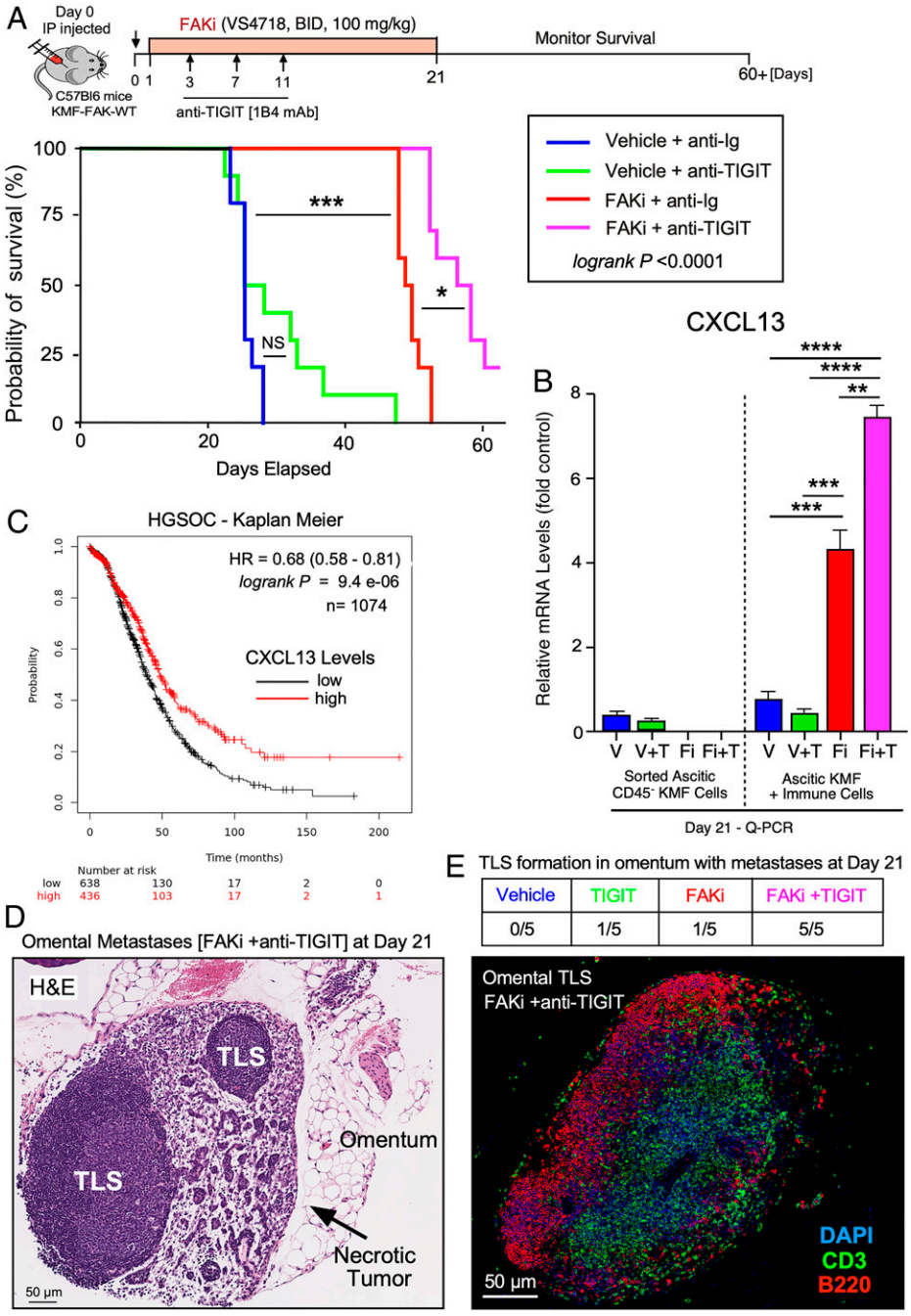

Fig. 5. Targeting FAK and TIGIT enhances survival and TLS formation. (*A*) Experimental schematic: same as Fig. 4. Experimental groups (n = 10 each) were oral vehicle plus anti-Ig (V, blue line), vehicle plus anti-TIGIT (V+T, green line), VS-4718 (Fi, red line), or FAKi plus anti-TIGIT (Fi+T, purple line). Anti-Ig or anti-TIGIT injections were performed on days 3, 7, and 11. At day 21, treatments were stopped, and mice were evaluated for tumor burden up to 60 d. Survival is percent of total for each experimental group. Log-rank (Mantel–Cox test) significance was determined between the groups ($P < 0.001$). Comparisons Fi to T (*$P < 0.05$) and Fi+T (***$P < 0.001$, Log-rank (Mantel–Cox test) were calculated using Prism (v8.0). NS, not significant. (*B*) Flow cytometry was used to sort ascitic CD45- KMF tumor cells at day 21, and CXCL13 mRNA levels were measured by reverse-transcriptase qPCR (RT-qPCR) in the indicated sorted and total cell populations. Transcript levels were calculated using the ΔΔCT method and normalized to RPL19 housekeeping gene. Values are means ± SEM from 3 mice per group (**$P < 0.01$, ***$P < 0.001$, ****$P < 0.0001$ one-way ANOVA with Tukey's multiple comparisons test). Data are representative of two independent experiments. (*C*) Kaplan-Meier analysis of CXCL13 mRNA levels in 1,074 HGSOC patient samples. The plot shows the probability of relapse-free survival in months with tumors high (red) or low (black) for CXCL13 mRNA (HR = 0.68, P = 9.4e-06). (*D*) Representative H&E image of omental tumor implant with TLS from FAKi plus anti-TIGIT treated mouse at day 21. (Scale bar, 50 µm.) (*E*) Quantitation of omental TLS-positive mice. Four sections per mouse at 100-µm intervals and 5 mice per group were analyzed in the indicated groups. Representative multiplex of anti-CD3 (green), anti-B220 (red), and DAPI (blue) nuclear staining of TLS in omentum from a FAKi plus anti-TIGIT treated mouse at day 21 is shown. (Scale bar, 50 µm.).

FAKi plus a TIGIT-blocking antibody prevented tumor growth and enhanced host survival with elevated CXCL13 levels and omental TLS formation. CXCL13 and TLS are markers of an antitumor immune response across several cancers (41) and HGSOC (43). Among all tumors, copy number gains in *PTK2* (the FAK gene) occur most frequently in HGSOC. FAK activity, reported by a validated phosphospecific antibody to active FAK (FAK pY576), was significantly elevated in stage III + IV HGSOC tumors and negatively correlated with CD3+ TIL staining. Tumor cells with high active FAK coexpressed CD155. In the KMF model, FAKi promoted T cell infiltration while decreasing Tregs, and the combination of FAKi plus anti-

TIGIT strongly prevented TIGIT expressing Treg infiltration. We observed tumor FAK activity to be a strong determinant of immunosuppression and that high levels of active FAK with CD155 in HGSOC tumors may indicate an immune evasive phenotype.

Both tumor-associated genetic and pharmacologic FAK inhibition triggered an increase in immune-cell-secreted CXCL13 expression and rendered tumors more responsive to TIGIT immunotherapy. In effect, the FAKi phenotype resembles that of agents that cause T cell priming and activation (44). Much work is still needed to understand how losses in FAK activity result in immune cell activation and how this may be linked to TLS formation or outcome. To this end, expression of selected chemokines, including CXCL13, is associated with TLS formation (40) and with improved HGSOC patient outcomes (37). In addition to regulating CD155, FAK inhibition also effectively suppressed CD45− tumor PD-L1 expression in vivo. However, as ID8 tumors (parental to KMF) are insensitive to anti-PD1 inhibition (4), FAKi plus anti-PD1 was not investigated in the KMF model. In this regard, KMF cells are a murine model with limited genetic similarity to HGSOC, and additional studies are needed to test potential connections between FAK and CD155 in other HGSOC and other tumor models.

Small-molecule inhibitors may have off-target effects in vivo as VS-4718 also inhibits the FAK homolog Pyk2 (27). However, we derived parallel results with tumor cells expressing catalytically inactive FAK, thus reinforcing the importance of tumor-intrinsic FAK signaling. Although FAK can promote immunosuppression in other cancers, the proposed mechanism(s) of action do not necessarily translate to HGSOC. In pancreatic cancer, FAK prevents immune cell infiltration in part via the regulation of tissue fibrosis (33, 45). In a squamous cell carcinoma model, tumor FAK activity promoted CD8+ T cell exhaustion and Treg recruitment via increased CCL5 chemokine expression (34). However, the role for increased CCL5 levels in HGSOC is complex, as increased CCL5 is conversely associated with TIL infiltration and immunotherapy responsiveness (46). The commonality between these and our studies is that targetable FAK activity drives tumor-immunosuppressive phenotypes. The combinatorial agents used with FAK inhibition may be tumor specific. Moreover, our HGSOC tumor staining results provide important spatial insights into areas of CD3 lymphocyte exclusion within tumors containing active FAK and CD155 costaining. The linkage between CD155 with active FAK and the presence of increased FAK activity together with decreased T cell infiltrates in stage III/IV disease suggest that FAK-mediated immune evasion may be linked to HGSOC spread.

Only a subset of HGSOC patients derive benefit from checkpoint inhibitor immunotherapies (7), although only selected checkpoint inhibitor pathways have been evaluated to date. Here, FAKi plus anti-TIGIT enhanced mouse survival in an aggressive platinum-resistant model of ovarian cancer, consistent with protocols combining FAKi with one or even multiple checkpoint inhibitors in other cancers (35). This provides compelling preclinical rationale for the combination of FAK inhibitor therapy with checkpoint inhibitors in HGSOC, which has been ranked among the most immunologically cold cancers (47). This translation is not only logical but also urgent and should be feasible given the combinatorial potential of FAK inhibitors and antibody therapies targeting the CD155/TIGIT axis currently in clinical trials.

Materials and Methods

Cells and Culture. Murine KMF, human 293T, and human A2780-CP70 ovarian carcinoma cells were used as described (26). For in vitro experiments, cells were treated with dimethyl sulfoxide (control) or 1 μM FAK inhibitor VS-4718 (Verastem).

Cloning and Mutagenesis. Mutagenesis to change murine FAK tyrosine (Y576) to phenylalanine (F576) was performed in PSB-tet RP FAK-WT by PCR amplification with CloneAmp (Takara, 639298) followed by In-Fusion cloning. Primer sequences used for PCR were as follows: forward, 5′CAGTACTTTCTAT AAAGCTTCCAAAGGAAAATTAC3′; and reverse, 5′TTATAGAAAGTACTGTCTTCCATATA TCGAG3′. GFP-FAK constructs in pCDH were cloned into SfiI sites in the doxycycline inducible Sleeping Beauty transposon expression vector PSBtet-RP (gift from Eric Kowarz, Addgene Plasmid 60497) using In-Fusion HD Cloning Plus (Takara, Japan) with the primers forward, 5′ttcctaccctcgaaaggcctctgaggccATGGTGA GCAAGGGCG3′; and reverse, 5′tatcgatggaagcttggcctgacaggccTCAGCGGCC GCACTGAG3′.

Tumor Growth. All animal experiments were performed in accordance with The Association for Assessment and Accreditation for Laboratory Animal Care guidelines and approved by the University of California San Diego (UCSD) Institutional Animal Care and Use Committee (protocol S07331). For KMF FAK-WT or KMF FAK-KD tumor growth and ascites analyses, 5 million pChili-luciferase-labeled cells in 100 μL Dulbecco's modified Eagle's medium were suspended with 100 μL phenol-red-free high concentration Matrigel (Corning, 354262) and IP injected into 8- to 10-wk-old female C57Bl6/N mice (Charles River). Tumor growth was monitored via bioluminescent luciferase imaging at indicated days (IVIS, Perkin-Elmer). A2780-CP70 tumor growth was evaluated by IP injection of 4 million pChili-Luciferase-labeled cells mixed with Matrigel into 9-wk-old female non-obese diabetic severe combined immune deficiency gamma mice (Jackson Laboratory) as described (26). Vehicle or VS-4718 FAK inhibitor (100 mg/kg) via oral gavage was administered BID.

Ascites and Peritoneal Cell Isolation. Mice were euthanized at indicated days and KMF tumorsphere plus peritoneal immune cells were harvested by injection of 5 mL Collection Buffer (phosphate buffer saline [PBS] containing 2 mM ethylenediaminetetraacetic acid [EDTA] and 2% bovine serum albumin [BSA]). Volume of up to 10 ml was collected, red blood cells were lysed (RBC lysis buffer, eBioscience, 00-4300-54) for 5 min at room temperature (RT), reactions were stopped by dilution with Collection Buffer at 4 °C, and cells were pelleted by centrifugation (2,000 rpm for 6 min at 4 °C). Cell pellets were resuspended in 2 mL PBS containing 4 mM EDTA and 2% BSA and mechanically dissociated by gentle and repeated pipetting (1,000-μL tip). Cells were diluted by addition of PBS with 2 mM EDTA and 2% BSA, filtered through a 70-μm cell strainer, and enumerated by a single-cell suspension, and cell viability (>90%) was verified by automated trypan blue dye exclusion (ViCell XR, Beckman).

FAKi and Anti-TIGIT Antibody Treatments. FAKi VS-4718 was suspended in 0.5% carboxymethyl cellulose (Sigma) and 0.1% Tween 80 (Sigma) in sterile water and administered BID (100 mg/kg) by oral gavage at day 1 through day 21. KMF-tumor-bearing mice were injected with low endotoxin anti-TIGIT (1B4-mAb, 200 μg) (38) or with Invivomab mouse IgG1 isotype control (200 μg, Bio X Cell, BE0083) at experimental days 3, 7, and 11 as indicated. Treatments were stopped at day 21, and mice were euthanized for analyses. For survival studies, mice after therapy cessation at day 21 were evaluated daily for ascites tumor burden (appearance and body mass increase) and interference of normal behavior (feeding, grooming, and lethargy) prior to humane euthanasia as defined by Institutional Animal Care and Use Committee (IACUC) guidelines.

Multispectral Flow Cytometry. Three million cells per experimental point were sequentially stained with Fc block for 15 min (BD Biosciences, 553141) and with fluorescent antibodies in 50 μL Brilliant Stain Buffer (BD Biosciences, 566349) for 30 min on ice. Samples were washed, fixed, and permeabilized using Foxp3/Transcription Factor Staining Buffer Set (eBioscience, 00-5523-00) according to the manufacturer's protocol. Foxp3 staining was performed after fixation and permeabilization. UltraComp eBeads (Invitrogen, 01-2222-42) were stained with antibodies for compensation controls. For gating, mouse

splenocytes were mixed with samples and used as positive and fluorescence minus one controls. Samples were analyzed using BD FACSCelesta or BD LSRFortessa flow cytometers. Data analysis used Flowlogic flow software (Miltenyi Biotec), and representative gating is shown in *SI Appendix*, Figs. S3 and S4.

RNA Extraction and NanoString. Total RNAs were extracted using the PureLink RNA Mini Kit (Thermo). nanoString hybridization was performed using the nCounter PanCancer Mouse Immune Profiling panel. A total of 770 genes including housekeeping genes were analyzed using nSolver 4.0 and Advanced Analysis 2.0 (48). For the T cell activity gene heatmap, normalized ratio and *P* values were calculated with a *t* test using nSolver for treatment (FAKi vs. vehicle) and genotype (FAK-KD vs. FAK-WT). Genes with at least a twofold increase in FAKi treated vs. vehicle samples and in FAK-KD vs. FAK-WT samples with a *P* value of $\leq$0.05 were analyzed. A total of 77 genes were identified and 33 were related to T cell activation gene set group as defined by nanoString cell type analysis. A heatmap was generated using GraphPad Prism (v8).

Quantitative RT-PCR. Total RNAs were extracted using the PureLink RNA Mini Kit (Thermo). cDNA was prepared using the High-Capacity cDNA Reverse Transcription Kit (Thermo) from 1 μg total RNA. Target transcripts were amplified using a LightCycler 480 (Roche Applied Science), and iTaq Universal SYBR Green Supermix (Bio-Rad) with cDNA template according to manufacturer instructions. Target gene expression was normalized to 60S ribosomal protein L19 (RPL19) as a housekeeping gene control. Transcript levels were calculated using the ΔΔCT (cycle threshold) method. Primer sequences used were as follows: musRPL19F, TGATCTGCTGACGGAGTTG; musRPL19R, GGAAAAGAAGGTCTGGTTGGA; musCXCL13F, CTCCAGGCCACGGTATTCTG; and musCXCL13R, CCAGGGGGCGTAACTTGAAT.

Kaplan-Meier. Expression array data were evaluated using the Kaplan-Meier Plotter (www.kmplot.com/ovar). The CXCL13 probe set [205242_at] was used, and query parameters were overall survival, auto-select best cutoff, with a follow up threshold of 10 y. The signal range of the probe was 1 to 6,274 and the auto-cutoff value was 161. Restriction analyses were Stage (2 + 3+4), serous histology (serous), all tumor grades, and no selection for surgery or chemotherapy treatments. A total of 1,064 samples were analyzed.

Transcriptome Analyses. For an analysis of mRNA expression, the ovarian cancer firehose legacy database (Broad Institute) was accessed via cBioportal (5/28/2021). *PTK2* (FAK) mRNA expression from 182 patients that were subject to RNAseq were binned into 3 groups of 60 to 61 patients based on ascending expression, and the mean quantity of CD3 mRNA isolated from that bin of tumors was derived. To determine the Pearson correlation between *PTK2* mRNA and the mRNA for the checkpoint ligands PD-L1 (CD274), PDCD1LG2 (CD273), PVR (CD155), PVRL2 (CD112), CD80, and CD86, the cBioportal integrative genomics viewer was used. The plot function (49) was used to evaluate expression in patients with elevated *PTK2*. Breast cancer (METABRIC database, 1,904 patients), pancreatic carcinoma (The Cancer Genome Atlas (TCGA) Firehose Legacy Database, 149 patients), lung carcinoma (TCGA Firehose Legacy Database, 230 patients), and neuroblastoma (TARGET data set, 141 patients) were analyzed, and comparisons were made to *PTK2* mRNA.

Statistics. Statistical difference between unpaired groups of 2 were performed using the nonparametric Mann–Whitney *U* test with groups of unequal numbers. When data were normally distributed, analyses were performed using an unpaired two-tailed Student's *t* test. Differences between groups of 3 or more were determined using one-way ANOVA with Tukey's multiple comparison. The log-rank test was used for survival analysis. All statistical analyses were performed using Prism (v8, GraphPad Software) or for nSolver Software for nanoString. *P* values of <0.05 were considered significant.

Data Availability. The NanoString Immune Profiler FASTQ data files have been deposited to the National Center for Biotechnology Information (NCBI) Gene Expression Omnibus (GEO) under the accession number GSE182726. Antibodies used and methods for immunohistochemistry, multiplex immunofluorescence, and quantitative image analysis can be found in *SI Appendix*. All other study data are included in the article and/or *SI Appendix*.

ACKNOWLEDGMENTS. We thank D. Hinz, C. Dillingham, and C. Kim at the La Jolla Institute for Immunology for flow cytometry expertise and D. Molina for the technical assistance with NanoString analyses. This study was supported by a Department of Defense (DOD) Ovarian Cancer Pilot Grant DOD W81XWH19101, NIH 1R01CA24756, NIH R01CA254342, and Nine Girls Ask? 501(c)(3). D.O. was supported by Ann and Sol Schreiber Mentored Investigator Award from the Ovarian Cancer Research Alliance (OCRA 650255) and by NIH training grant (T32-CA121938). M.O. was supported by a Sigrid Juselius Foundation Fellowship (Finland). A.M.B. was a Gaines Gynecologic Oncology Fellow in the Division of Gynecologic Oncology at UCSD. The Zeiss LSM880 at the La Jolla Institute for Immunology Light Microscopy Core was supported by NIH S10OD021831. The UCSD Tissue Technology Shared Resource is supported by NIH P30CA23100. Murine anti-TIGIT (1B4) blocking antibody generation was supported by P01 AI039671 (Core B). nanoString analyses were supported in part by the CIRM Major Facilities Grant (FA1-00607) to the Sanford Consortium for Regenerative Medicine.

Author affiliations: [a]Department of Obstetrics, Gynecology, and Reproductive Sciences, Moores University of California San Diego (UCSD) Cancer Center, La Jolla, CA 92093; [b]Department of Surgery, Moores UCSD Cancer Center, La Jolla, CA 92093; [c]State Key Laboratory of Cellular Stress Biology, School of Medicine, Xiamen University, Xiamen, Fujian 361102, China; [d]Department of Pathology, Moores UCSD Cancer Center, La Jolla, CA 92093; [e]Microscopy Core, La Jolla Institute for Immunology, La Jolla, CA 92037; [f]Developmental Therapeutics Program, Fox Chase Cancer Center, Philadelphia, PA 19111; [g]Chief Scientific Officer, Verastem Oncology, Needham, MA, 02494; and [h]Evergrande Center, Brigham and Women's Hospital, Harvard Medical School, Boston, MA 02115

Author contributions: D.O., J.S.S.N., V.E., D.G.S. and D.D.S. designed research; D.O., J.S.S.N., J.A., M.O., A.M.B., S.J., S.I., X.L.C., M.R., T.B., Z.M., and D.G.S. performed research; J.A.P. and V.K.K. contributed new reagents/analytic tools; D.O., J.S.S.N., J.A., M.O., A.M.B., X.L.C., V.E., A.M., Z.M., M.C.M., R.R.W., D.C.C., V.K.K., D.G.S., and D.D.S. analyzed data; and D.O., D.G.S., and D.D.S. wrote the paper.

1. R. L. Siegel, K. D. Miller, H. E. Fuchs, A. Jemal, Cancer statistics, 2021. *CA Cancer J. Clin.* **71**, 7–33 (2021).
2. U. A. Matulonis *et al.*, Ovarian cancer. *Nat. Rev. Dis. Primers* **2**, 16061 (2016).
3. P. P. Santoiemma, D. J. Powell Jr., Tumor infiltrating lymphocytes in ovarian cancer. *Cancer Biol. Ther.* **16**, 807–820 (2015).
4. K. Odunsi, Immunotherapy in ovarian cancer. *Ann. Oncol.* **28**, viii1–viii7 (2017).
5. S. C. Wei, C. R. Duffy, J. P. Allison, Fundamental mechanisms of immune checkpoint blockade therapy. *Cancer Discov.* **8**, 1069–1086 (2018).
6. E. Barber, D. Matei, Immunotherapy in ovarian cancer: We are not there yet. *Lancet Oncol.* **22**, 903–905 (2021).
7. S. Morand, M. Devanaboyina, H. Staats, L. Stanbery, J. Nemunaitis, Ovarian cancer immunotherapy and personalized medicine. *Int. J. Mol. Sci.* **22**, 6532 (2021).
8. A. Ribas, J. D. Wolchok, Cancer immunotherapy using checkpoint blockade. *Science* **359**, 1350–1355 (2018).
9. A. J. Anandappa, C. J. Wu, P. A. Ott, Directing traffic: How to effectively drive T cells into tumors. *Cancer Discov.* **10**, 185–197 (2020).
10. A. C. Anderson, N. Joller, V. K. Kuchroo, Lag-3, Tim-3, and TIGIT: Co-inhibitory receptors with specialized functions in immune regulation. *Immunity* **44**, 989–1004 (2016).
11. Q. Zhang *et al.*, Blockade of the checkpoint receptor TIGIT prevents NK cell exhaustion and elicits potent anti-tumor immunity. *Nat. Immunol.* **19**, 723–732 (2018).
12. S. Kurtulus *et al.*, TIGIT predominantly regulates the immune response via regulatory T cells. *J. Clin. Invest.* **125**, 4053–4062 (2015).
13. R. J. Johnston *et al.*, The immunoreceptor TIGIT regulates antitumor and antiviral CD8(+) T cell effector function. *Cancer Cell* **26**, 923–937 (2014).
14. J. Gao, Q. Zheng, N. Xin, W. Wang, C. Zhao, CD155, an onco-immunologic molecule in human tumors. *Cancer Sci.* **108**, 1934–1938 (2017).
15. B. L. Solomon, I. Garrido-Laguna, TIGIT: A novel immunotherapy target moving from bench to bedside. *Cancer Immunol. Immunother.* **67**, 1659–1667 (2018).
16. L. Wu *et al.*, Blockade of TIGIT/CD155 signaling reverses T-cell exhaustion and enhances antitumor capability in head and neck squamous cell carcinoma. *Cancer Immunol. Res.* **7**, 1700–1713 (2019).
17. W. A. Freed-Pastor *et al.*, The CD155/TIGIT axis promotes and maintains immune evasion in neoantigen-expressing pancreatic cancer. *Cancer Cell* **39**, 1342–1360.e14 (2021).
18. J. Smazynski *et al.*, The immune suppressive factors CD155 and PD-L1 show contrasting expression patterns and immune correlates in ovarian and other cancers. *Gynecol. Oncol.* **158**, 167–177 (2020).
19. E. Dolgin, Antibody engineers seek optimal drug targeting TIGIT checkpoint. *Nat. Biotechnol.* **38**, 1007–1009 (2020).
20. Z. Alteber *et al.*, Therapeutic targeting of checkpoint receptors within the DNAM1 axis. *Cancer Discov.* **11**, 1040–1051 (2021).
21. J. M. Balko, J. A. Sosman, A critical need for better cancer immunotherapy models: Are organotypic tumor spheroid cultures the answer? *Cancer Discov.* **8**, 143–145 (2018).
22. C. W. McCloskey, G. M. Rodriguez, K. J. C. Galpin, B. C. Vanderhyden, Ovarian cancer immunotherapy: Preclinical models and emerging therapeutics. *Cancers (Basel)* **10**, 244 (2018).
23. S. Zhang *et al.*, Genetically defined, syngeneic organoid platform for developing combination therapies for ovarian cancer. *Cancer Discov.* **11**, 362–383 (2021).
24. S. Iyer *et al.*, Genetically defined syngeneic mouse models of ovarian cancer as tools for the discovery of combination immunotherapy. *Cancer Discov.* **11**, 384–407 (2021).
25. K. F. Roby *et al.*, Development of a syngeneic mouse model for events related to ovarian cancer. *Carcinogenesis* **21**, 585–591 (2000).
26. C. J. Diaz Osterman *et al.*, FAK activity sustains intrinsic and acquired ovarian cancer resistance to platinum chemotherapy. *eLife* **8**, e47327 (2019).

27. J. C. Dawson, A. Serrels, D. G. Stupack, D. D. Schlaepfer, M. C. Frame, Targeting FAK in anticancer combination therapies. *Nat. Rev. Cancer* **21**, 313–324 (2021).
28. F. J. Sulzmaier, C. Jean, D. D. Schlaepfer, FAK in cancer: Mechanistic findings and clinical applications. *Nat. Rev. Cancer* **14**, 598–610 (2014).
29. H. Zhang *et al.*; CPTAC Investigators, Integrated proteogenomic characterization of human high-grade serous ovarian cancer. *Cell* **166**, 755–765 (2016).
30. C. Jean *et al.*, Inhibition of endothelial FAK activity prevents tumor metastasis by enhancing barrier function. *J. Cell Biol.* **204**, 247–263 (2014).
31. S. Zaghdoudi *et al.*, FAK activity in cancer-associated fibroblasts is a prognostic marker and a druggable key metastatic player in pancreatic cancer. *EMBO Mol. Med.* **12**, e12010 (2020).
32. F. Demircioglu *et al.*, Cancer associated fibroblast FAK regulates malignant cell metabolism. *Nat. Commun.* **11**, 1290 (2020).
33. H. Jiang *et al.*, Targeting focal adhesion kinase renders pancreatic cancers responsive to checkpoint immunotherapy. *Nat. Med.* **22**, 851–860 (2016).
34. A. Serrels *et al.*, Nuclear FAK controls chemokine transcription, Tregs, and evasion of anti-tumor immunity. *Cell* **163**, 160–173 (2015).
35. M. Canel *et al.*, T-cell co-stimulation in combination with targeting FAK drives enhanced anti-tumor immunity. *eLife* **9**, e48092 (2020).
36. E. L. Goode *et al.*; Ovarian Tumor Tissue Analysis (OTTA) Consortium, Dose-response association of $CD8^+$ tumor-infiltrating lymphocytes and survival time in high-grade serous ovarian cancer. *JAMA Oncol.* **3**, e173290 (2017).
37. M. Yang *et al.*, CXCL13 shapes immunoactive tumor microenvironment and enhances the efficacy of PD-1 checkpoint blockade in high-grade serous ovarian cancer. *J. Immunother. Cancer* **9**, e001136 (2021).
38. K. O. Dixon *et al.*, Functional anti-TIGIT antibodies regulate development of autoimmunity and antitumor immunity. *J. Immunol.* **200**, 3000–3007 (2018).
39. E. J. Wherry, M. Kurachi, Molecular and cellular insights into T cell exhaustion. *Nat. Rev. Immunol.* **15**, 486–499 (2015).
40. T. N. Schumacher, D. S. Thommen, Tertiary lymphoid structures in cancer. *Science* **375**, eabf9419 (2022).
41. C. Sautès-Fridman, F. Petitprez, J. Calderaro, W. H. Fridman, Tertiary lymphoid structures in the era of cancer immunotherapy. *Nat. Rev. Cancer* **19**, 307–325 (2019).
42. V. H. Engelhard *et al.*, Immune cell infiltration and tertiary lymphoid structures as determinants of antitumor immunity. *J. Immunol.* **200**, 432–442 (2018).
43. D. R. Kroeger, K. Milne, B. H. Nelson, Tumor-infiltrating plasma cells are associated with tertiary lymphoid structures, cytolytic T-cell responses, and superior prognosis in ovarian cancer. *Clin. Cancer Res.* **22**, 3005–3015 (2016).
44. J. Galon, D. Bruni, Approaches to treat immune hot, altered and cold tumours with combination immunotherapies. *Nat. Rev. Drug Discov.* **18**, 197–218 (2019).
45. H. Laklai *et al.*, Genotype tunes pancreatic ductal adenocarcinoma tissue tension to induce matricellular fibrosis and tumor progression. *Nat. Med.* **22**, 497–505 (2016).
46. D. Dangaj *et al.*, Cooperation between constitutive and inducible chemokines enables T cell engraftment and immune attack in solid tumors. *Cancer Cell* **35**, 885–900.e10 (2019).
47. J. N. Kather *et al.*, Topography of cancer-associated immune cells in human solid tumors. *eLife* **7**, e36967 (2018).
48. A. Cesano, nCounter(®) PanCancer Immune Profiling Panel (NanoString Technologies, Inc., Seattle, WA). *J. Immunother. Cancer* **3**, 42 (2015).
49. J. Gao *et al.*, Integrative analysis of complex cancer genomics and clinical profiles using the cBioPortal. *Sci. Signal.* **6**, pl1 (2013).
50. P. Bankhead *et al.*, QuPath: Open source software for digital pathology image analysis. *Sci. Rep.* **7**, 16878 (2017).